ACS APPLIED MATERIALS & INTERFACES

www.acsami.org

Research Article

Self-Polymerized Dopamine-Decorated Au NPs and Coordinated with Fe-MOF as a Dual Binding Sites and Dual Signal-Amplifying Electrochemical Aptasensor for the Detection of CEA

Jifan Li,[§] Lei Liu,[§] Yongjian Ai, Yang Liu, Hongbin Sun,* and Qionglin Liang*

Cite This: *ACS Appl. Mater. Interfaces* 2020, 12, 5500−5510

Read Online

ACCESS | Metrics & More | Article Recommendations | Supporting Information

ABSTRACT: Fabrication of functional electrochemical biosensor is a hot topic; however, precise and sensitive cancer detection in early clinical diagnosis is still a great challenge. Continuous efforts have been devoted to explore functional materials for this issue. In this work, we developed a dual binding sites and dual signal-amplifying electrochemical aptasensor of self-polymerized dopamine-decorated Au and coordinated with Fe-MOF (Au@PDA@Fe-MOF) for the detection of carcinoembryonic antigen (CEA). Remarkably, Au@PDA@Fe-MOF features high sensitivity, multiple active sites, good biocompatibility, and excellent selectivity, which is attributed to abundant −COOH in porous Fe-MOF and unsaturated Fe^{3+} sites on the surface of Fe-MOF as the active binding sites grafting more NH_2-functionalized CEA-specific aptamer and redox PDA and Fe-MOF accelerating the movement of electrons for dual signal amplifying. Meanwhile, the electrochemical aptasensor shows favorable repeatability with 1.82% relative standard deviation (RSD) under five independent aptasensors and strong stability with only 3.3% degradation after 12 days of storage. In addition, the aptasensor has wide CEA detection range from 1 fg mL^{-1} to 1 μg mL^{-1} with a low detection limit of 0.33 fg mL^{-1} (S/N = 3). Furthermore, the aptasensor is feasible for accurate and quantitative detection of CEA in serum samples with RSD below 2.32%. The satisfying results demonstrate promising applications of the CEA aptasensor in practical sample analysis and lay an important foundation for other biomarker detection in early clinical diagnosis.

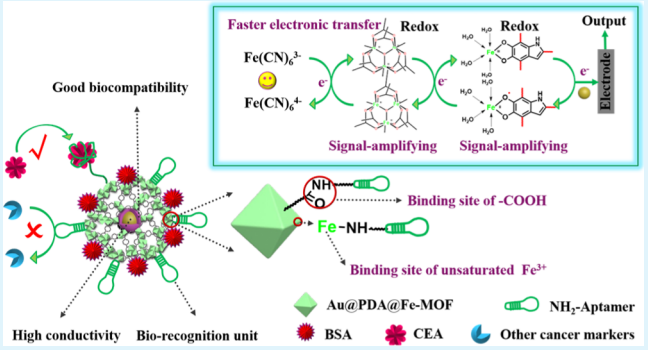

KEYWORDS: *carcinoembryonic antigen, electrochemical aptasensor, Au@PDA@Fe-MOF, dual binding sites, dual signal amplifying*

INTRODUCTION

Nowadays, people are scared of cancer for the extremely high mortality rate.[1] One of the main reasons for the poor survival rate of cancer is the later diagnosis and once founded to be advanced stage. Therefore, the early and precise detection of cancer, which is vital for clinical diagnosis, and real-time monitoring along with effective treatment can significantly reduce mortality and save lives.[2] At present, a great deal of efforts has been devoted to explore various promising detection methods based on the specific recognition of cancer biomarkers. Carcinoembryonic antigen (CEA) as a most widely used clinical tumor marker overexpressed in colorectal cancer,[3] pancreatic,[4] breast,[5] cervical carcinoma,[6] cystadenocarcinoma,[7] and others. Therefore, developing an accurate, convenient, and sensitive detection method for CEA detection is crucial, which can diagnose earlier and improve survival rate markedly.

CEA detection methods include polymerase chain reaction,[2] enzyme-linked immunosorbent assay (ELISA),[8] surface-enhanced Raman spectroscopy, electrophoresis,[9] surface plasmon resonance,[10] electrochemical assay,[11] colorimetric assay,[12] fluorescence methods,[13] and so forth. These detection methods are abundant and highly efficient. Among these means, the electrochemical detection method is widely used in biomarker detection due to its innate high sensitivity, simplicity, miniaturization, real-time monitoring, and so on.[14,15] In recent years, aptasensors have received a lot of attention owing to the specific binding to their corresponding target molecules with high affinity.[16] Aptamer that is able to bind with the target molecule noncovalently has been used as ideal recognition elements in the biosensing field.[17] Aptamers have prominent advantages, such as simplicity, good chemistry stability, repeatability, high selectivity, and low cost, which are superior to antibodies.[18−20] Currently, novel electrochemical aptasensors have been widely used to detect CEA with the advantage of high sensitivity, simplicity and fast response.[21,22]

Received: October 29, 2019
Accepted: January 15, 2020
Published: January 15, 2020

https://dx.doi.org/10.1021/acsami.9b19161
ACS Appl. Mater. Interfaces 2020, 12, 5500−5510

Scheme 1. Schematic Representation for the Preparation Process (a) and the Functioning Mechanism (b) of Au@PDA@Fe-MOF and Electrochemical Aptasensor for CEA Detection

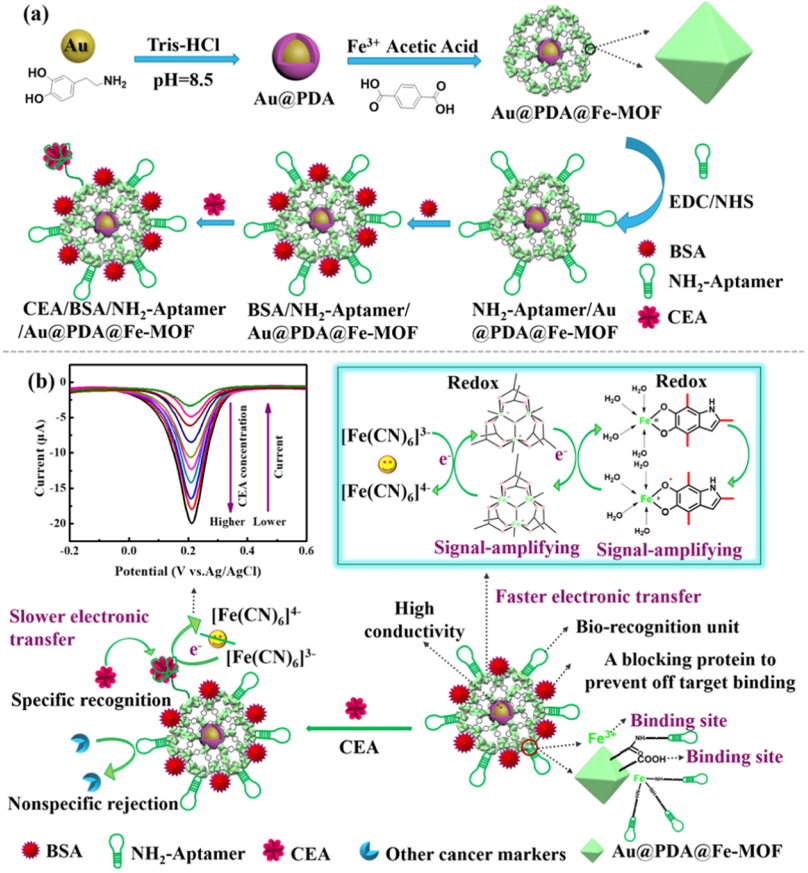

To date, aptamers are assembled with the redox nanomaterials as label-free sensors, which can amplify signals for improving the detection sensitivity in a biosensor assay. Furthermore, hybrid bio/nano-structures hold great promise in amplifying signals to increase the sensitivity of a biosensor and bringing forth higher accuracy and precision.[2] Thus, the functional materials with redox property for dual amplifying signals will be more beneficial for the sensitive detection of CEA.

Metal−organic frameworks (MOFs) consisting of metal ions and organic ligands[23,24] have recently emerged as a promising candidate that attract considerable attention for application in electrochemical sensing[25] by their various grafting groups (e.g., $-NH_2$ or −COOH),[26] $\pi-\pi$ stacking, hydrogen bonding, and electrostatic interactions with negatively charged nucleic acid sequences,[27] for example, some redox MOFs including Co-MOF,[28] Ce-MOF,[29] Fe-MOF,[30] Ru-MOF,[31] and so forth. Among various MOF materials, Fe-based MOFs (Fe-MOFs) stand out for that iron is an earth-abundant element and these MOFs possess excellent stability, nontoxic property, and redox activity with abundant Fe centers in their crystalline structure. Despite that MOFs have many merits, MOF-based aptasensors still suffer from poor conductivity, and the dual binding sites of Fe-MOFs have scarcely been concerned.

Owing to these demands in advanced materials and our interest, we designed a dual binding sites and dual signal amplifying electrochemical aptasensor of self-polymerized dopamine (DA)-decorated Au NPs and coordinated with Fe-MOF (Au@PDA@Fe-MOF), which possess high sensitivity, good biocompatibility, high selectivity, and strong stability. Gold (Au) nanoparticles, a high conductive material, have been favored as a biosensor material with excellent chemical stability, biocompatibility, and catalytic activity.[32,33] DA, as a redox surface modifier for adhesion function to amplify signal,[33] has wide application in cancer therapy[34] due to its strong adhesive properties, biocompatibility,[35] and PDA modification.[36,37] The self-polymerizing of DA on the surface of Au nanoparticles can not only regulate the size of Au nanoparticles but also ensure the strong interaction with biomolecules, which has excellent biocompatibility.[38] On the one hand, there are abundant −COOH in porous Fe-MOF and unsaturated Fe^{3+} sites on the surface of Fe-MOF as the active sites, which lead to expose more sites for grafting the NH_2-functionalized CEA-specific aptamer. On the other hand, the redox PDA and Fe-MOF can accelerate the movement of electrons, which ultimately improves the electrochemical signal and sensitivity toward the determination of CEA. The preparation process of the electrochemical aptasensor was illustrated in Scheme 1.

EXPERIMENTS SECTION

Regents and Apparatus. More information about the regents and apparatus were provided in Supporting Information.

Preparation of Au Nanoparticles (Au NPs). Globular Au nanoparticles of 13 nm were prepared by reducing $HAuCl_4$ with trisodium citrate based on previously reported literature.[39] First, 55 μL of 9 wt % $HAuCl_4$ was added into 49.95 mL of ultrapure water and refluxed at boiling. Then, adding 0.75 mL of sodium citrate (10 mg mL^{-1}) as a reducing agent, the mixture was continuously stirred for 15 min. A wine red uniformly dispersed solution containing Au NPs

https://dx.doi.org/10.1021/acsami.9b19161
ACS Appl. Mater. Interfaces 2020, 12, 5500−5510

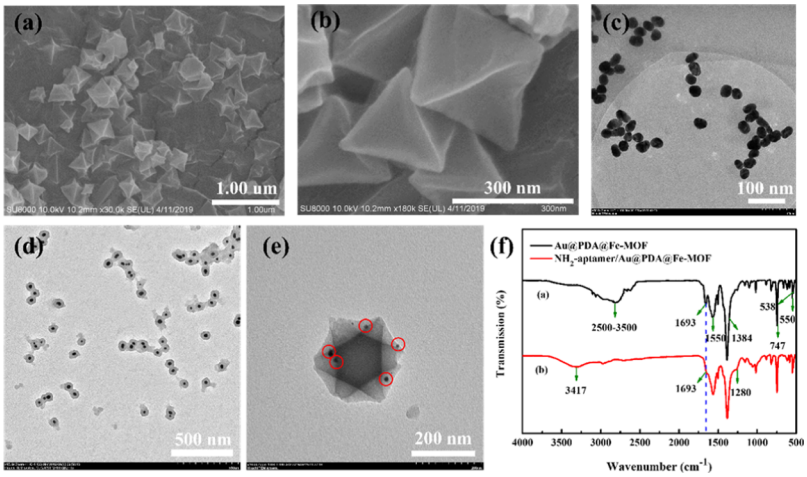

Figure 1. SEM images of Au@PDA@Fe-MOF (a,b), TEM images of Au (c), Au@PDA (d), Au@PDA@Fe-MOF (e), and FTIR spectrum (f) of Au@PDA@Fe-MOF and NH_2-aptamer/Au@PDA@Fe-MOF.

was obtained. At last, 50 mL of as-synthesized Au nanoparticles (20 nm) was centrifuged at 12 000 rpm for 15 min, and then, the precipitates were redispersed in 2 mL of ultrapure water.

Preparation of Au@PDA. The Au NPs prepared above were decorated with DA, which were modified with the previously reported procedures.[40] The condensed Au NPs (500 μL) were added dropwise in a clean conical flask containing 16 mL of Tris buffer (0.1 mol/L, pH = 8.5) under constant stirring, and then 3-hydroxytyramine hydrochloride was added in the mixture for 0.2 mg mL^{-1}. The mixed solution was stirred for 18 h and centrifuged with ethanol and ultrapure water to obtain the dark product. At last, the purified Au@PDA was redispersed in 2 mL of ultrapure water.

Synthesis of Au@PDA@Fe-MOF. We synthesized the functional material of Au@PDA@Fe-MOF. Au@PDA (0.5 mL) was dissolved in 15.0 mL of *N*,*N*-dimethylformamide (DMF), and iron(III) chloride hexahydrate ($FeCl_3{\cdot}6H_2O$, 0.35 mmol L^{-1}) and 1,4-dicarboxybenzene acid (H_2BDC, 0.76 mmol L^{-1}) were added to the mixture in order. The samples were dissolved in DMF by ultrasound and dispersed uniformly. Under the ultrasonic condition, 0.5 mL of acetic acid was then added dropwise into this mixed solution. The mixture was heated and stirred in an oil bath at 120 °C and refluxed for 4 h to crystallize it. Then, the product Au@PDA@Fe-MOF was collected through centrifugation and washed with DMF and ethanol three times to remove the excess reactants. Finally, the purified Au@PDA@Fe-MOF nanocomposite was vacuum freeze-dried.

Preparation of the MOF-Based Aptasensor. Self-polymerized DA-decorated Au NPs and coordinated with Fe-MOF as a dual binding sites and dual signal-amplifying electrochemical aptasensor was prepared as illustrated in Scheme 1a, and the mechanism for the reaction process was elaborated in Schemes 1b and S1. Under the condition of oxygen and alkaline condition, the monomers of DA were oxidized and rearranged to the intermediate of polydopamine and coated on the surface of Au nanoparticles uniformly. Then, PDA provided anchoring sites for Fe^{3+} to form Fe^{3+}−catechol complexes, owing to their strong coordination capability. Finally, under the precursor of H_2BDC, they formed octahedrons. Among the reaction process, acetic acid, as a regulator, plays an important role of increasing the number of −COOH and regulating the nucleation and growth rate of MOFs.[41−43] Then, the NH_2-aptamer was covalently binding with abundant −COOH in porous Fe-MOF and sufficient unsaturated Fe sites on the surface of Fe-MOF based on *N*-ethylcarbodiimide/*N*-hydroxysuccinimide (EDC/NHS) coupling. The strong Fe(III)−N bond is on a par with typical covalent bonds.[44] The successful conjugation of NH_2-aptamer with Au@PDA@Fe-MOF was confirmed by Fourier-transform infrared spectroscopy (FTIR) (Figure 1f), X-ray photoelectron spectroscopy (XPS, Figure 3), and electrochemical behavior (Figure 5).

The functioning mechanism of the prepared aptasensor was clearly described in Scheme 1b. Au@PDA@Fe-MOF has the merits of high sensitivity, multiple active sites, the high conductivity of Au NPs, good biocompatibility, excellent selectivity, and redox PDA and Fe-MOF for dual signal amplifying. On the one hand, the prepared aptasensor has sufficient COOH in porous Fe-MOF and unsaturated Fe^{3+} sites on the surface of Fe-MOF as the active binding sites to graft with the NH_2-functionalized CEA-specific aptamer for the sensitive detection of CEA, which can expand the detection range and increase the sensitivity markedly. On the other hand, the redox PDA and Fe-MOF can accelerate the electron transfer on the electrode interface of $[Fe(CN)_6]^{3-/4-}$, which will amplify the signals of current. Generally speaking, signal amplifying leads to enhancement of sensitivity.[45] Before detection, the electrode of Au@PDA@Fe-MOF was modified by EDC/NHS to activate COOH, and then the active COOH and unsaturated Fe^{3+} will graft with a biological recognition unit of NH_2-aptamer. Bovine serum albumin (BSA), as blocking protein, was then covered on the electrode to prevent off-target binding. Finally, specific recognition of NH_2-aptamer and CEA can be used to select binding-specific proteins, and the nonspecific antigen will not be binding to NH_2-aptamer. Once the NH_2-aptamer bind with CEA, a protein layer will be formed on the electrode surface, which will obstruct the electron transfer of $[Fe(CN)_6]^{3-/4-}$ and the current of differential pulse voltammetry (DPV) will be reduced. The current will decrease gradually with the increase of the CEA concentration.

Before modification, the glassy carbon electrode (GCE) was polished with alpha alumina slurry (1.0, 0.3, and 0.05 μm) to obtain a mirror-like clean surface and then dried by nitrogen. Au@PDA@Fe-MOF (1 mg) was added to a mixture solution of 10 μL of 5% w/w Nafion, 590 mL ethanol, and 460 mL deionized water, and then, the suspension was sonicated for 30 min. The homogenous suspension (5 μL) was dripped on the surface of GCE to obtain a modified Au@PDA@Fe-MOF/GCE electrode. After being dried at room temperature, 10 μL of EDC/NHS (150 mmol L^{-1} EDC, 100 mmol L^{-1} NHS) mixture solution was added dropwise onto the Au@PDA@Fe-MOF/GCE electrode and stored in a 4 °C refrigerator for 1 h to activate −COOH groups in porous Fe-MOF. Subsequently, 8 μL of 3.5 μg mL^{-1} (3.5 μM) specific NH_2-aptamer solution of CEA was grafted for 50 min to obtain the NH_2-aptamer/Au@PDA@Fe-MOF/GCE electrode and rinsed in phosphate-buffered saline (PBS) to remove physically absorbed NH_2-aptamer. Then, the modified electrode was covered by 40 μL of 0.05% BSA for 30 min at 4 °C to cover the unspecific binding sites. Then, the BSA/NH_2-aptamer/Au@PDA@Fe-MOF/GCE electrode was formed and washed with PBS thoroughly. Ultimately, the prepared BSA/NH_2-aptamer/Au@PDA@Fe-MOF/GCE electrode was incubated with 40 μL of CEA solution of different concentrations for 35 min at 4 °C and then washed thoroughly with PBS to wash off nonspecifically bound

https://dx.doi.org/10.1021/acsami.9b19161
ACS Appl. Mater. Interfaces 2020, 12, 5500−5510

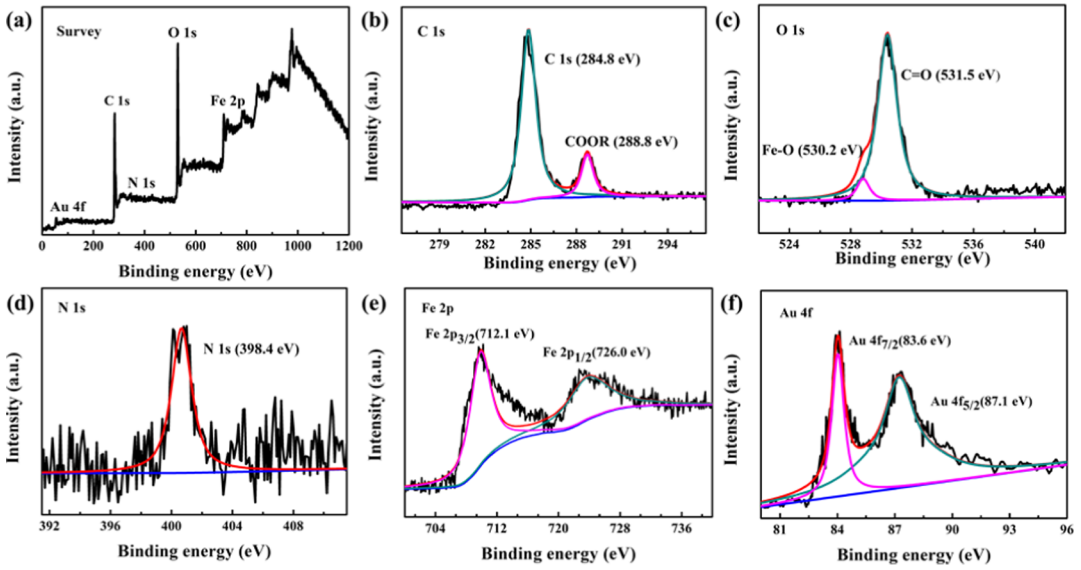

Figure 2. XPS spectra of Au@PDA@Fe-MOF. (a) Survey, (b) C 1s, (c) O 1s, (d) N 1s, (e) Fe 2p, and (f) Au.

conjugations. The resulting CEA/BSA/NH_2-aptamer/Au@PDA@Fe-MOF/GCE aptasensor was used for later electrochemical measurements, such as the electrochemical behaviors of the each step modification of the aptasensor were studied by electrochemical impedance spectroscopy (EIS) and cyclic voltammograms (CV) in Figure 5.

RESULTS AND DISCUSSION

Characterization of the Au@PDA@Fe-MOF. The morphologies were observed by scanning electron microscopy (SEM) and transmission electron microscopy (TEM). As presented in Figure 1a,b, SEM of Au@PDA@Fe-MOF exhibits a regular concave octahedral shape with 8 facets and 12 edges, and the side length was 240 nm. As shown in Figure 1c,d, the size of citrate-stabilized Au NPs was 13 nm and Au NPs were successfully coated by DA without aggregating in Figure 1d. During polymerization, PDA formed an inerratic and continuous coating layer at the surface of Au via the strong binding affinity of catechol functional groups. From Figure 1e, the uniform star-like profile with an octahedral sketch was observed, which was consistent with the SEM image. Au NP (13 nm) was observed in Fe-MOF (Figure 1e) but not on the surface of Fe-MOF (Figure 1a,b), indicating that Au NP was encapsulated in Fe-MOF. The X-ray diffraction (XRD) patterns in Figure S1 also proved the successful synthesis of Au@PDA@Fe-MOF.

Au@PDA@Fe-MOF (a) and NH_2-aptamer/Au@PDA@Fe-MOF (b) were analyzed by FTIR spectroscopy in Figure 1f to study the molecular structure and chemical bond. The FTIR spectrum of H_2BDC is in Figure S2, and the regions of 2551−3054 cm^{-1} are matched to the typical wide vibrational bands of the O−H association peak from the carboxylic acid. The peak at 1693 cm^{-1} represents the C═O stretching of the free carboxyl group, while 1550 cm^{-1} means the carboxyl group that coordinated to the Fe metal centers (Figure 1f). As shown in Figure 1f, the peak at 1693 cm^{-1} represents the C═O stretching of the free carboxyl group and the disappeared C═O results from the covalent binding with NH_2-aptamer. The result illustrated that Au@PDA@Fe-MOF had adequate COOH as binding sites to graft NH_2-aptamer. The broad absorption about 1300 cm^{-1} indicated water and/or other gases, which have been adsorbed in the frameworks. The similar phenomenon for some other MOFs has been reported by Tan, et al.[46] The adsorption band at 1101 cm^{-1} refers to O−H deformation in plane (Figure S2). Moreover, FTIR signals at 747, 550, and 538 cm^{-1} in Figure 1f (curve a) are corresponding to the C−H bending vibrations of the benzene rings, the vibration band of strong Fe−O[47] and Fe−O on benzene rings, respectively. Such differences of Au@PDA@Fe-MOF and H_2BDC demonstrated the coordination of the bridging ligand with Fe and the formation of metal−oxo bond. After binding with the NH_2-aptamer, the characteristic peaks of the amide bond[48] can be observed in Figure 1f (curve b): FTIR signals at 1280 and 3417 cm^{-1} represent the stretching vibration of P═O from NH_2-aptamer and N−H from HN−C═O. These results confirmed that NH_2-aptamers were successfully grafted with Au@PDA@Fe-MOF.

XPS was conducted to study the surface chemical composition of Au@PDA@Fe-MOF. The XPS survey spectrum (Figure 2a) proved that C, O, N, Fe, and Au elements coexist in Au@PDA@Fe-MOF. As shown in Figure 2b, the spectrum of the C 1s displayed two surface components, which are corresponding to carbon components on the benzene ring (284.7 eV) and carboxylate (COOR) groups from the H_2BDC linkers (288.6 eV).[49,50] The spectrum of the O 1s was fitted into two peaks (Figure 2c), which were located at the binding energies (BEs) of 530.2 and 531.5 eV corresponding to C═O and Fe−O bonds of Fe-MOF,[51] and the oxygen components on BDC linkers,[52] respectively. The spectrum of the N 1s (Figure 2d) from PDA was fitted to the BE of 398.4 eV, which also proved the binding of the catechol groups to the Au NP surface.[53,54] Figure 2e shows a high-resolution XPS spectrum of the Fe 2p with the content of 6.47%. As XPS is a means of surface analysis, a great deal of unsaturated Fe sites on the surface of Fe-MOF can be used to graft NH_2-aptamer. The typical peaks at 712.1 eV were ascribed to Fe $2p_{3/2}$ and peaks at 726.0 eV were assigned to Fe $2p_{1/2}$.[55] The high-resolution XPS spectrum of the Au was fixed at Au $4f_{5/2}$ (83.6 eV) and Au $4f_{7/2}$ (87.1 eV) in Figure 2f.[38]

To further confirm the successful binding of Au@PDA@Fe-MOF with NH_2-aptamer, XPS of NH_2-aptamer/Au@PDA@Fe-MOF was conducted in Figure 3. The XPS survey spectrum

https://dx.doi.org/10.1021/acsami.9b19161
ACS Appl. Mater. Interfaces 2020, 12, 5500−5510

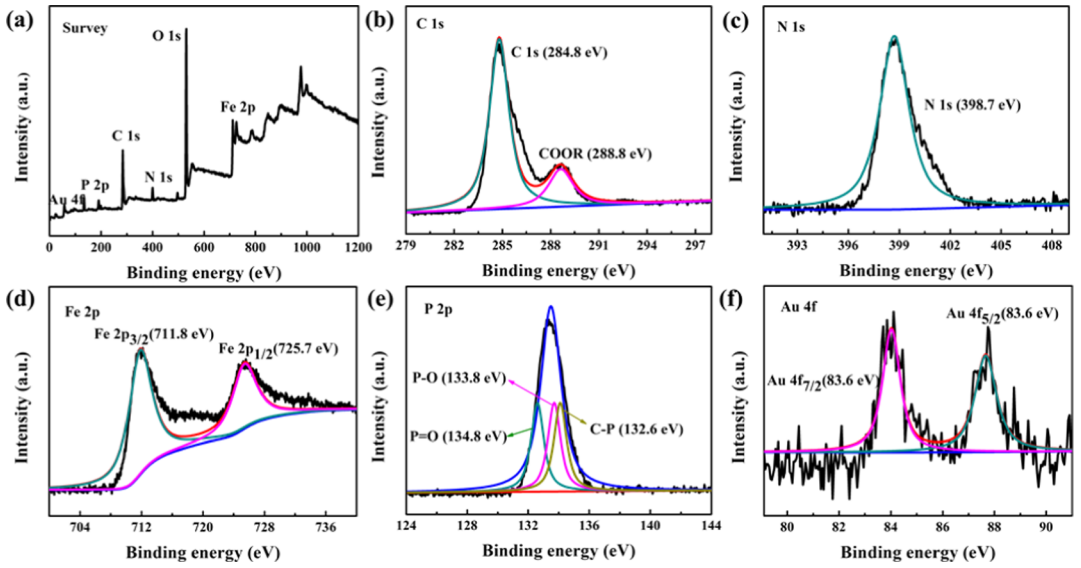

Figure 3. XPS spectra of NH_2-aptamer/Au@PDA@Fe-MOF. (a) Survey, (b) C 1s, (c) N 1s, (d) Fe 2p, (e) P 2p, and (f) Au.

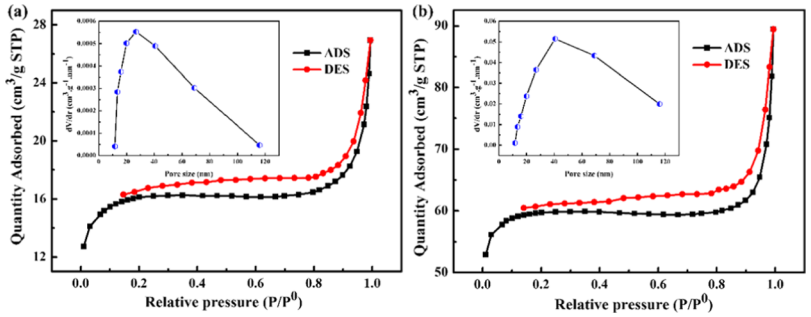

Figure 4. N_2 adsorption/desorption isotherms of (a) NH_2-aptamer/Au@PDA@Fe-MOF and (b) Au@PDA@Fe-MOF. Inset: corresponding pore size distribution.

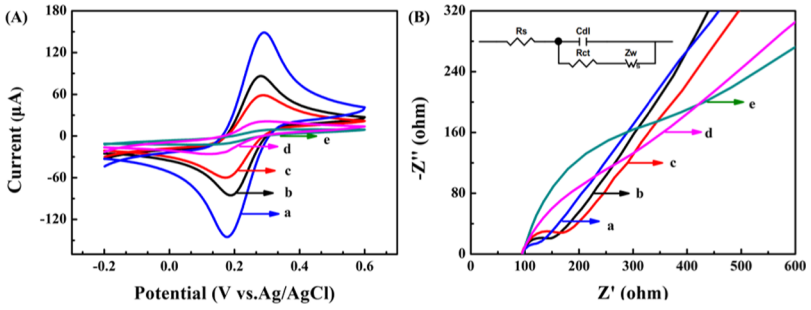

Figure 5. (A) CV and (B) EIS response of (a) Au@PDA@Fe-MOF/GCE, (b) bare GCE, (c) NH_2-aptamer/Au@PDA@Fe-MOF/GCE, (d) BSA/NH_2-aptamer/Au@PDA@Fe-MOF/GCE, and (e) CEA/BSA/NH_2-aptamer/Au@PDA@Fe-MOF/GCE in 0.10 M KCl electrolyte solution containing 5 mM $K_3Fe(CN)_6/K_4Fe(CN)_6$ as redox indicator. The corresponding equivalent circuits are inserted in (B).

(Figure 3a) indicated that NH_2-aptamer/Au@PDA@Fe-MOF contained C, O, N, Fe, Au, and P elements. The presence of P element (Figure 3e) and the increase of N element (Figure 3c) from NH_2-aptamer proved the successful binding of Au@PDA@Fe-MOF and NH_2-aptamer. It was worth noting that the two BEs at 711.8 and 725.7 eV of Fe (Figure 3d) acting as the electron acceptor had reduced 0.3 eV comparing to 712.1 and 726.0 eV of Fe (Figure 2e). However, the BEs at 398.7 eV of N (Figure 3c) acting as the electron donor had increased 0.3 eV comparing to 398.4 eV of N (Figure 2d), which illustrated the coordination of unsaturated Fe^{3+} sites on the surface of Fe-MOF with NH_2-aptamer. The XPS and FTIR results together proved that Au@PDA@Fe-MOF as dual binding sites were feasible and promising to graft NH_2-aptamer for the sensitive detection of CEA.

The specific surface area and porosity of the samples were characterized by nitrogen-sorption measurements. As shown in Figure 4, NH_2-aptamer/Au@PDA@Fe-MOF (Figure 4a) and Au@PDA@Fe-MOF (Figure 4b) exhibited typical type I isotherms with a H_4 hysteresis loop according to IUPAC's classification. NH_2-aptamer/Au@PDA@Fe-MOF had a lower Brunauer–Emmett–Teller surface area (54.7622 m^2 g^{-1}) than Au@PDA@Fe-MOF (199.8562 m^2 g^{-1}), indicating the

https://dx.doi.org/10.1021/acsami.9b19161
ACS Appl. Mater. Interfaces 2020, 12, 5500–5510

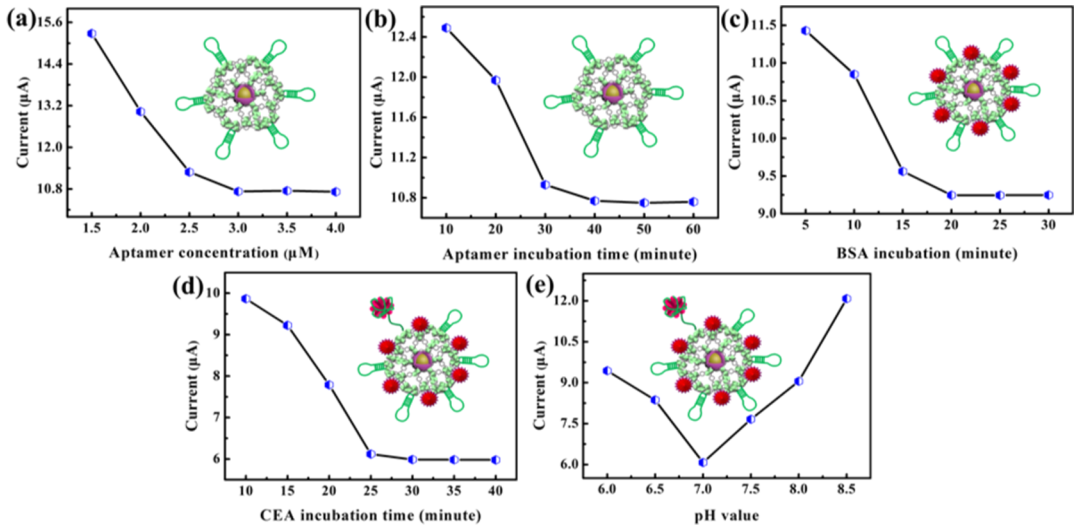

Figure 6. Effect of (a) aptamer concentration, (b) aptamer incubation time, (c) BSA covering time, (d) CEA (10 ng mL^{-1}) incubation time, and (e) pH value.

successful grafting of NH_2-aptamer, and this may block the flexible pores of Fe-MOF.

Electrochemistry Behaviors of Aptasensor. The CV and EIS results of layer-by-layer assembled materials are shown in Figure 5. In Figure 5A, Au@PDA@Fe-MOF/GCE (Figure 5a) had a great conducting ability with a larger reversible redox peak in CV than that of the bare GCE (Figure 5b), which was attributed to the redox couple of PDA[56] and Fe-MOF[57] as the electroactive species accelerating the electro transfer process of the redox probe $\{[Fe(CN)_6]^{3-/4-}\}$[58] on the electrode surface. The mechanism was elaborated in Schemes 1b and S1. Then, the Au@PDA@Fe-MOF was modified by EDC/NHS to carboxylated −COOH in porous Fe-MOF MOF. The peak current of NH_2-aptamer/Au@PDA@Fe-MOF/GCE (Figure 5c) also decreased when NH_2-aptamer was covalently fixed to COOH in the porous Fe-MOF and coordinated to unsaturated Fe^{3+} site on the surface of Fe-MOF, that is because the grafted negative charge aptamer with phosphate groups repelled the negative redox probes and blocked electron transfer to the electrode surface.[59] Then, the NH_2-aptamer/Au@PDA@Fe-MOF/GCE-modified electrode was covered with BSA to cover the unspecific sites on the sensor interface. Figure 5d shows that the peak current declined after the covering of BSA because BSA as an insulating layer can prevent electron migration to the electrode interface.[60] Finally, the peak current of CEA/BSA/NH_2-aptamer/Au@PDA@Fe-MOF/GCE aptasensor (Figure 5e) was further reduced for capturing CEA (10 ng mL^{-1}), which formed a protein layer on the electrode surface and changed the steric barrier.[61]

EIS is made up of a semicircle part representing for finite electron transfer and a linear part on behalf of the diffusion limited process to monitor electrode interface properties during the electrochemical aptasensor construction processes.[62] The corresponding equivalent circuits are inserted in Figure 5B. The electron-transfer resistance (R_{et}) of Au@PDA@Fe-MOF (Figure 5a, 40 Ω) was much smaller than those of bare GCE (Figure 5b, 60.3 Ω), NH_2-aptamer/Au@PDA@Fe-MOF (Figure 5c, 81.5 Ω), BSA/NH_2-aptamer/Au@PDA@Fe-MOF (Figure 5d, 299.8 Ω), and CEA/BSA/NH_2-aptamer/Au@PDA@Fe-MOF (Figure 5e, 402.2 Ω) under optimal conditions. As the electrode is gradually modified, R_{et} increases (Figure 5B). That was in good agreement with CV analysis. The smaller impedance was attributed to the dual redox electroactive PDA and Fe-MOF, which accelerated the electro transfer of $[Fe(CN)_6]^{3-/4-}$ on the electrode surface and enhanced electrochemical signal. The experimental results show that the dual signal amplifying aptasensor was effectively constructed, and the electrochemical aptasensor had good performance.

Optimization of the Analytical Conditions. The immobilization condition of the aptamer has an important influence on the performance of the sensor. Therefore, we had optimized the grafting concentration and grafting time of NH_2-aptamer, the covering time of BSA, the incubation time of CEA, and the pH value of PBS buffer solution successively under DPV measurement for the merits of low background current, high detection sensitivity, and low detection limit.

First, we optimized the concentration of the NH_2-aptamer, and the Au@PDA@MOF/GCE electrodes were incubated with different concentration of NH_2-aptamer solution (1.5−4.0 μM) for the same time. As shown in Figure 6a, the electrochemical signal decreased sharply with increasing concentration of CEA aptamer below 3 μM owing to the negative charge of NH_2-aptamer, which can increase steric hindrance and make it difficult to the electron transfer of $[Fe(CN)_6]^{4-/3-}$ on the electrode surface,[63] and the electrochemical signal had insignificant difference with increasing concentration of NH_2-aptamer above 3 μM for the saturation equilibrium. Therefore, 3.5 μM was chosen as the optimal concentration of NH_2-aptamer because there will be too many unspecific sites in CEA biosensor fabrication at lower concentration, but when the concentration is too high, it may cause a big background interference owing to more nonspecific adsorptions.[64]

In order to further investigate the influence of the grafting time of NH_2-aptamer, the NH_2-aptamer/Au@PDA@MOF/GCE electrodes were incubated with different times (10−60 min) of 3.5 μM NH_2-aptamer and then tested by DPV. In Figure 6b, the electrochemical signal decreased evidently with the increasing grafting time of NH_2-aptamer from 10 to 40 min, and the electrochemical signal became almost the same

https://dx.doi.org/10.1021/acsami.9b19161
ACS Appl. Mater. Interfaces 2020, 12, 5500−5510

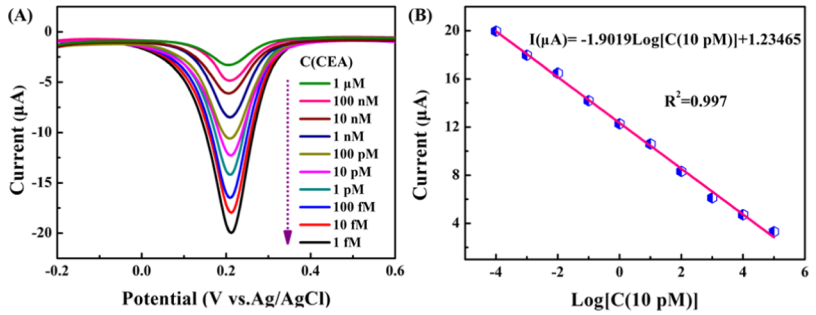

Figure 7. (A) DPV response of BSA/NH_2-aptamer/Au@PDA@Fe-MOF/GCE aptasensor after incubating with different concentration of CEA (1 fM to 1 μM); (B) Calibration curve for CEA detection.

with the time continued. Thus, the grafting time of NH_2-aptamer was set as 50 min for saving time.

Generally, BSA was used for covering the unspecific sites on the sensor interface. The NH_2-aptamer/Au@PDA@MOF/GCE electrodes were incubated in BSA solution for different times and followed by DPV detection. The results showed that the curve remains stable after 20 min (Figure 6c). Therefore, 25 min was selected as the optimal covering time of BSA. The reason was that there will be too many uncovered nonspecific binding sites on the surface under insufficient time resulting in an inaccurate detection results, but when the time exceeds 20 min, it will form the "insulating layer" hindering the diffusion of electroactive substance and the electron transfer on the sensing interface.

The incubation time of CEA (10 ng mL^{-1}) was also studied by adjusting the different incubation time of BSA/NH_2-aptamer/Au@PDA@MOF/GCE electrodes from 10 to 40 min. As illustrated in Figure 6d, the electricity showed a rapid reduction with time going from 10 to 30 min and nearly remained unchanged after 30 min. The results suggested that 35 min was a binding saturation between CEA and NH_2-aptamer.[65] Therefore, 35 min was selected as the optimal CEA incubation time of the electrochemical sensing detection.

The pH value of PBS buffer solution has a significant influence on the electrochemical performance of the aptasensor because the highly acidic or alkaline environment affect the biological activity of the immobilized protein[66] and reduce the specific recognition of CEA and NH_2-aptamer, which will lead to a high current. As shown in Figure 6e, the signal response rapidly reduced with pH increasing from 6.0 to 7.0 and sharply increased with pH increasing from 7.0 to 8.5. Thus, pH 7.0 was selected as the optimal pH with the minimal current density for binding the maximum CEA, which was near the pH of the human body.

Electrochemical Detection of CEA. Different concentrations of CEA were measured by an electrochemical aptasensor under optimized conditions. As shown in Figure 7A, DPV curves responded to the different concentrations of CEA (1 fM to 1 μM), and the peak current decreased successively with the increase of CEA concentration. There was a good linear relationship between the peak current and CEA concentration of 1 fM to 1 μM (Figure 7B), and the linear regression equation was I (μA) = −1.9019 log[C (10 pM)] + 1.23465 in which the correlation coefficient is 0.99739. Limit of detection (LOD) was 0.33 fg mL^{-1} (S/N = 3). Compared with some previously reported methods (Table S1), our aptasensor has significant advantages in relatively wider linear range and lower detection limit for redox PDA and Fe-MOF as the electroactive species for dual signal amplifying. Meanwhile, these analysis parameters also proved that the electrochemical aptasensor can be used for quantitative detection of CEA.

Electrochemical Detection of CEA. The reproducibility test of the aptasensor was further evaluated in Figure 8a. Five independent aptasensors were used to detect CEA (10 ng mL^{-1}) under optimal conditions. The relative standard deviation (RSD) obtained was about 1.82%, indicating that the changes in the detection results of different sensors can be

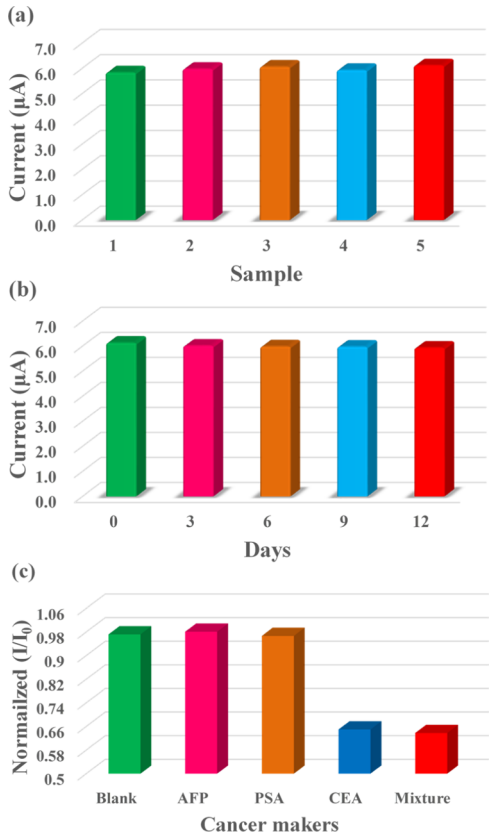

Figure 8. (a)Reproducibility of the BSA/Aptamer/Au@PDA@Fe-MOF/GCE sensor was examined by detecting 10 ng mL^{-1} of CEA with five independent aptasensors at the same analysis condition. (b) Stability of the aptasensor was examined by detecting 10 ng mL^{-1} of CEA with different storage time. (c) Selectivity of the electrochemical aptasensor to CEA compared with interfering cancer makers. The concentration of the proteins: 200 ng mL^{-1} AFP and 200 ng mL^{-1} PSA, 200 ng mL^{-1} AFP, 200 ng mL^{-1} PSA, 10 ng mL^{-1} CEA and 10 ng mL^{-1} CEA mixed with 200 ng mL^{-1} AFP and 200 ng mL^{-1} PSA, respectively.

https://dx.doi.org/10.1021/acsami.9b19161
ACS Appl. Mater. Interfaces 2020, 12, 5500−5510

ignored. This value was much lower than that in the literature studies.[67] Furthermore, the aptasensor was stored in 4 °C refrigerator for 12 days to study the stability. As shown in Figure 8b, the peak current slightly reduced by 3.3% of the original value after 12 days of storage with the same experimental conditions. Besides, the stability of the electrochemical biosensor in the detection process was studied in Figure S3. During the test, the stable signal before and after 100 cycles suggests that the materials modified on the electrode surface did not change. The results showed that the electrochemical aptasensor had strong stability.

The selectivity of the aptasensor was also important, and it can be evaluated by detecting some potential interferers, such as prostate-specific antigen (PSA, 200 ng mL^{-1}) and alpha-fetoprotein (AFP, 200 ng mL^{-1}). In this study, 200 ng mL^{-1} PSA, 200 ng mL^{-1}AFP, 10 ng mL^{-1} CEA mixed with 200 ng mL^{-1} PSA, and 200 ng mL^{-1} AFP were used as the control groups, and 200 ng mL^{-1} PSA together with 200 ng mL^{-1} AFP was used as the blank control group. As can be seen from Figure 8c, the current response of the CEA and CEA mixture were almost the same value but far lower than other solutions, which indicated that the aptasensor possesses an excellent selectivity in detecting CEA. The high selectivity of the aptasensor was attributed to the high specificity of molecular recognition between the aptamer and corresponding antigen. The inspiring results demonstrated that the prepared aptasensor can be used to detect CEA in complex serum samples with high reproducibility, stability, sensitivity, and specificity.

Control Experiment. The control experiment was carried out to prove the availability of the aptasensor for CEA detection. First, the carboxyl Au@PDA@Fe-MOF (Figure 9a)

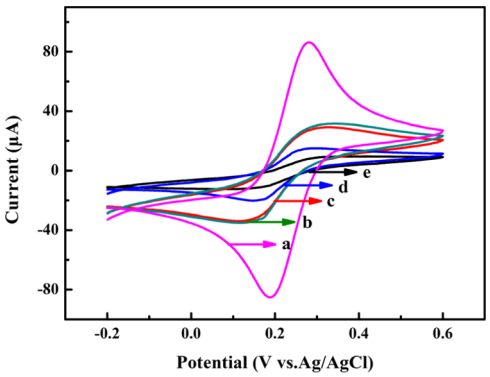

Figure 9. CV signals for (a) Au@PDA@Fe-MOF/GCE, (b) BSA/Au@PDA@Fe-MOF/GCE, (c) CEA/BSA/Au@PDA@Fe-MOF/GCE, (d) BSA/NH_2-aptamer/Au@PDA@Fe-MOF/GCE, (e) CEA/BSA/NH_2-aptamer/Au@PDA@Fe-MOF/GCE, respectively.

was covered by BSA directly without the modifying of the NH_2-aptamer. After 30 min of covering with BSA, the CV test was conducted on the prepared BSA/Au@PDA@Fe-MOF/GCE (Figure 9b). The peak current of CEA/BSA/Au@PDA@Fe-MOF/GCE (Figure 9c) was approximately equal to BSA/Au@PDA@Fe-MOF/GCE. The change of current before and after the incubation of CEA was not obvious without the modifying of NH_2-aptamer. However, the peak current of BSA/NH_2-aptamer/Au@PDA@Fe-MOF/GCE (Figure 9d) was significantly changed after incubation with 10 ng mL^{-1} CEA (Figure 9e). The results proved that the decrease of current of BSA/NH_2-aptamer/Au@PDA@Fe-MOF/GCE was caused by the binding of NH_2-aptamer and CEA. When the NH_2-aptamer binds to the CEA molecule, a protein formed on the surface of the electrode, which led to slower electron transfer and decreased peak current.

CEA Detection in Human Serum Samples. Whether human serum samples can be accurately analyzed is an important indicator of electrochemical biosensors. In order to evaluate the applicability of the electrochemical aptasensor, the CEA concentration in the original human serum sample was determined to be 0.3 ng mL^{-1} by ELISA method first, and then the standard addition method was adopted to detect the recovery of CEA in the human serum samples. The detection results listed in Table 1 showed that the recovery ratio was

Table 1. Detection of CEA in Diluted Human Serum Samples (n = 3) with the As-Fabricated Electrochemical Aptasensor

$C_{initial}$ (ng mL^{-1})	serum sample	C_{added} (ng mL^{-1})	$C_{measured}$ (ng mL^{-1})	recovery (%)	RSD (%, n = 3)
0.30	1	1.00	1.33	102.3	1.57
	2	5.00	5.26	99.2	1.64
	3	50.00	50.84	101.1	2.32

ranging from 99.2 to 102.3% with RSD below 2.32%, indicating that it is feasible for accurate and quantitative detection of CEA in serum samples. Thus, the aptasensor possess excellent sensing performance, including high sensitivity, excellent selectivity, strong stability, and good reproducibility, and can be effectively applied to the clinical detection.

CONCLUSIONS

In summary, a dual binding sites and dual signal-amplifying electrochemical aptasensor of self-polymerized DA decorated Au and coordinated with Fe-MOF (Au@PDA@Fe-MOF) for the detection of CEA was constructed. This aptasensor has excellent electrochemical performance because of good bioaffinity, high sensitivity, multiple active sites, good biocompatibility, and excellent selectivity. Under optimal conditions, the aptasensor had wide linear concentration range of 1 fg mL^{-1} to 1 μg mL^{-1}, and LOD as low as 0.33 fg mL^{-1} (S/N = 3). Concurrently, the electrochemical aptasensor also owns superior sensitivity and selectivity, good reproducibility, high stability, and satisfactory applicability in human serum. Therefore, the electrochemical aptasensor provides a feasible platform for biomarker detection in early clinical diagnosis.

ASSOCIATED CONTENT

Supporting Information

The Supporting Information is available free of charge at https://pubs.acs.org/doi/10.1021/acsami.9b19161.

Regents and apparatus, reaction mechanism, XRD of Au@PDA@Fe-MOF, FTIR spectrum of H_2BDC, stability of electrochemical biosensor in the detection process, and comparison of different methods for the determination of CEA and reference (PDF)

https://dx.doi.org/10.1021/acsami.9b19161
ACS Appl. Mater. Interfaces 2020, 12, 5500−5510

AUTHOR INFORMATION

Corresponding Authors

Hongbin Sun − *Department of Chemistry, Northeastern University, Shenyang 110819, People's Republic of China;* orcid.org/0000-0002-9007-4091; Email: sunhb@mail.neu.edu.cn

Qionglin Liang − *Key Laboratory of Bioorganic Phosphorus Chemistry & Chemical Biology (Ministry of Education), Department of Chemistry, Center for Synthetic and Systems Biology, Tsinghua University, Beijing 100084, People's Republic of China;* orcid.org/0000-0002-6750-038X; Email: liangql@tsinghua.edu.cn

Authors

Jifan Li − *Key Laboratory of Bioorganic Phosphorus Chemistry & Chemical Biology (Ministry of Education), Department of Chemistry, Center for Synthetic and Systems Biology, Tsinghua University, Beijing 100084, People's Republic of China; Department of Chemistry, Northeastern University, Shenyang 110819, People's Republic of China*

Lei Liu − *Department of Chemistry, Northeastern University, Shenyang 110819, People's Republic of China*

Yongjian Ai − *Key Laboratory of Bioorganic Phosphorus Chemistry & Chemical Biology (Ministry of Education), Department of Chemistry, Center for Synthetic and Systems Biology, Tsinghua University, Beijing 100084, People's Republic of China*

Yang Liu − *Key Laboratory of Bioorganic Phosphorus Chemistry & Chemical Biology (Ministry of Education), Department of Chemistry, Center for Synthetic and Systems Biology, Tsinghua University, Beijing 100084, People's Republic of China;* orcid.org/0000-0003-0042-5183

Complete contact information is available at: https://pubs.acs.org/10.1021/acsami.9b19161

Author Contributions

[§]J.L. and L.L. contribute equally.

Notes

The authors declare no competing financial interest.

ACKNOWLEDGMENTS

This work was financially supported by the National Natural Science Foundation of China (nos. 81872835, 21872020 and 21621003), the Ministry of Science and Technology (nos. 2017YFC0906902 and 2017ZX09301032), and the China Scholarship Council (no. 201806085012) is also acknowledged.

REFERENCES

(1) Penny, L. K.; Wallace, H. M. The Challenges for Cancer Chemoprevention. *Chem. Soc. Rev.* **2015**, *44*, 8836−8847.

(2) He, M.-Q.; Wang, K.; Wang, W.-J.; Yu, Y.-L.; Wang, J.-H. Smart DNA Machine for Carcinoembryonic Antigen Detection by Exonuclease III-Assisted Target Recycling and DNA Walker Cascade Amplification. *Anal. Chem.* **2017**, *89*, 9292−9298.

(3) Miao, J.; Wang, X.; Lu, L.; Zhu, P.; Mao, C.; Zhao, H.; Song, Y.; Shen, J. Electrochemical Immunosensor Based on Hyperbranched Structure for Carcinoembryonic Antigen Detection. *Biosens. Bioelectron.* **2014**, *58*, 9−16.

(4) Steward, A. M.; Nixon, D.; Zamcheck, N.; Aisenberg, A. Carcinoembryonic Antigen in Breast Cancer Patients: Serum Levels and Disease Progress. *Cancer* **1974**, *33*, 1246−1252.

(5) Huang, K.-J.; Niu, D.-J.; Xie, W.-Z.; Wang, W. A Disposable Electrochemical Immunosensor for Carcinoembryonic Antigen Based on Nano-Au/Multi-Walled Carbon Nanotubes-Chitosans Nanocomposite Film Modified Glassy Carbon Electrode. *Anal. Chim. Acta* **2010**, *659*, 102−108.

(6) Qiu, Z.; Shu, J.; Tang, D. Near-Infrared-to-Ultraviolet Light-Mediated Photoelectrochemical Aptasensing Platform for Cancer Biomarker Based on Core Shell NaYF4:Yb,Tm@TiO_2 Upconversion Microrods. *Anal. Chem.* **2018**, *90*, 1021−1028.

(7) Tang, J.; Tang, D.; Niessner, R.; Chen, G.; Knopp, D. Magneto-Controlled Graphene Immunosensing Platform for Simultaneous Multiplexed Electrochemical Immunoassay Using Distinguishable Signal Tags. *Anal. Chem.* **2011**, *83*, 5407−5414.

(8) de la Rica, R.; Stevens, M. M. Plasmonic ELISA for the Ultrasensitive Detection of Disease Biomarkers with the Naked Eye. *Nat. Nanotechnol.* **2012**, *7*, 821−824.

(9) Garcia-Schwarz, G.; Santiago, J. G. Rapid High-Specificity microRNA Detection Using a Two-stage Isotachophoresis Assay. *Angew. Chem., Int. Ed.* **2013**, *52*, 11534−11537.

(10) Krishnan, S.; Mani, V.; Wasalathanthri, D.; Kumar, C. V.; Rusling, J. F. Attomolar Detection of a Cancer Biomarker Protein in Serum by Surface Plasmon Resonance Using Superparamagnetic Particle Labels. *Angew. Chem., Int. Ed.* **2011**, *50*, 1175−1178.

(11) Gu, X.; She, Z.; Ma, T.; Tian, S.; Kraatz, H.-B. Electrochemical Detection of Carcinoembryonic Antigen. *Biosens. Bioelectron.* **2018**, *102*, 610−616.

(12) Song, Y.; Wei, W.; Qu, X. Colorimetric Biosensing Using Smart Materials. *Adv. Mater.* **2011**, *23*, 4215−4236.

(13) Miao, H.; Wang, L.; Zhuo, Y.; Zhou, Z.; Yang, X. Label-Free Fluorimetric Detection of CEA Using Carbon Dots Derived from Tomato Juice. *Biosens. Bioelectron.* **2016**, *86*, 83−89.

(14) Park, S. J.; Taton, T. A.; Mirkin, C. A. Array-Based Electrical Detection of DNA with Nanoparticle Probes. *Science* **2002**, *295*, 1503−1506.

(15) Wang, Z.; Liu, J.; Liang, Q.; Wang, Y.; Luo, G. Carbon Nanotube-Modified Electrodes for the Simultaneous Determination of Dopamine and Ascorbic Acid. *Analyst* **2002**, *127*, 653−658.

(16) Zhang, Z.; Guo, C.; Zhang, S.; He, L.; Wang, M.; Peng, D.; Tian, J.; Fang, S. Carbon-Based Nanocomposites with Aptamer-Templated Silver Nanoclusters for the Highly Sensitive and Selective Detection of Platelet-Derived Growth Factor. *Biosens. Bioelectron.* **2017**, *89*, 735−742.

(17) Sun, H.; Zu, Y. Aptamers and Their Applications in Nanomedicine. *Small* **2015**, *11*, 2352−2364.

(18) Meng, H.-M.; Liu, H.; Kuai, H.; Peng, R.; Mo, L.; Zhang, X.-B. Aptamer-Integrated DNA Nanostructures for Biosensing, Bioimaging and Cancer Therapy. *Chem. Soc. Rev.* **2016**, *45*, 2583−2602.

(19) Zhou, Z.-M.; Feng, Z.; Zhou, J.; Fang, B.-Y.; Qi, X.-X.; Ma, Z.-Y.; Liu, B.; Zhao, Y.-D.; Hu, X.-B. Capillary Electrophoresis-ChemiluminesCence Detection for Carcino-Embryonic Antigen Based on Aptamer/Graphene Oxide Structure. *Biosens. Bioelectron.* **2015**, *64*, 493−498.

(20) Yang, S.; Zhang, F.; Wang, Z.; Liang, Q. A Graphene Oxide-Based Label-Free Electrochemical Aptasensor for the Detection of Alpha-Fetoprotein. *Biosens. Bioelectron.* **2018**, *112*, 186−192.

(21) Khang, H.; Cho, K.; Chong, S.; Lee, J. H. All-In-One Dual-Aptasensor Capable of Rapidly Quantifying Carcinoembryonic Antigen. *Biosens. Bioelectron.* **2017**, *90*, 46−52.

(22) Zhang, Z.; Dong, L.; Zhu, Q. Rational Engineering of Synergically Stabilized Aptamer-cDNA Duplex Probes for Strand Displacement Based Electrochemical Sensors. *Electrochim. Acta* **2018**, *282*, 588−594.

(23) Wan, W.; Liang, Q.; Zhang, X.; Yan, M.; Ding, M. Magnetic Metal-Organic Frameworks for Selective Enrichment and Exclusion of Proteins for MALDI-TOF MS Analysis. *Analyst* **2016**, *141*, 4568−4572.

(24) Zhang, X.; Liang, Q.; Han, Q.; Wan, W.; Ding, M. Metal-Organic Frameworks@Graphene Hybrid Aerogels for Solid-Phase

Extraction of Nonsteroidal Anti-Inflammatory Drugs and Selective Enrichment of Proteins. *Analyst* **2016**, *141*, 4219−4226.
(25) Qiu, S.; Zhu, G. Molecular Engineering for Synthesizing Novel Structures of Metal-Organic Frameworks with Multifunctional Properties. *Coord. Chem. Rev.* **2009**, *253*, 2891−2911.
(26) Hou, W.; Liu, Y.; Zhang, B.; He, X.; Li, H. Electron Microscopy Visualization of Vitronectin Adsorbed on -COOH and -NH_2 Functionalized Surfaces: Distinctive Spatial Alignment and Regulated Cellular Responses. *Adv. Mater. Interfaces* **2017**, *4*, 1700958.
(27) Xie, B.-P.; Qiu, G.-H.; Hu, P.-P.; Liang, Z.; Liang, Y.-M.; Sun, B.; Bai, L.-P.; Jiang, Z.-H.; Chen, J.-X. Simultaneous Detection of Dengue and Zika Virus RNA Sequences with a Three-Dimensional Cu-Based Zwitterionic Metal-Organic Framework, Comparison of Single and Synchronous Fluorescence Analysis. *Sens. Actuators, B* **2018**, *254*, 1133−1140.
(28) Dai, L.; Li, Y.; Wang, Y.; Luo, X.; Wei, D.; Feng, R.; Yan, T.; Ren, X.; Du, B.; Wei, Q. A Prostate-Specific Antigen Electrochemical Immunosensor Based on Pd Nps Functionalized Electroactive Co-MOF Signal Amplification Strategy. *Biosens. Bioelectron.* **2019**, *132*, 97−104.
(29) Yu, H.; Han, J.; An, S.; Xie, G.; Chen, S. Ce(III, IV)-MOF Electrocatalyst as Signal-Amplifying Tag for Sensitive Electrochemical Aptasensing. *Biosens. Bioelectron.* **2018**, *109*, 63−69.
(30) Zhang, Z.; Ji, H.; Song, Y.; Zhang, S.; Wang, M.; Jia, C.; Tian, J.-Y.; He, L.; Zhang, X.; Liu, C.-S. Fe(III)-Based Metal-Organic Framework-Derived Core-Shell Nanostructure: Sensitive Electrochemical Platform for High Trace Determination of Heavy Metal Ions. *Biosens. Bioelectron.* **2017**, *94*, 358−364.
(31) Bao, C.; Fan, D.; Liu, X.; Wang, X.; Wu, D.; Ma, H.; Hu, L.; Wang, H.; Sun, X.; Wei, Q. A Signal-Off Type Photoelectrochemical Immunosensor for the Ultrasensitive Detection of Procalcitonin: $Ru(Bpy)_3^{2+}$ and Bi_2S_3 Co-Sensitized $Zntio_3/Tio_2$ Polyhedra as Matrix and Dual Inhibition By Sio_2/PDA-Au. *Biosens. Bioelectron.* **2019**, *142*, 111513.
(32) Wongkaew, N.; Simsek, M.; Griesche, C.; Baeumner, A. J. Functional Nanomaterials and Nanostructures Enhancing Electrochemical Biosensors and Lab-On-a-Chip Performances: Recent Progress, Applications, and Future Perspective. *Chem. Rev.* **2019**, *119*, 120−194.
(33) Black, K. C. L.; Liu, Z.; Messersmith, P. B. Catechol Redox Induced Formation of Metal Core-Polymer Shell Nanoparticles. *Chem. Mater.* **2011**, *23*, 1130−1135.
(34) Ku, S. H.; Ryu, J.; Hong, S. K.; Lee, H.; Park, C. B. General Functionalization Route for Cell Adhesion on Non-Wetting Surfaces. *Biomaterials* **2010**, *31*, 2535−2541.
(35) Liu, X.; Cao, J.; Li, H.; Li, J.; Jin, Q.; Ren, K.; Ji, J. Mussel-Inspired Polydopamine: A Biocompatible and Ultrastable Coating for Nanoparticles in Vivo. *ACS Nano* **2013**, *7*, 9384−9395.
(36) Lee, H.; Dellatore, S. M.; Miller, W. M.; Messersmith, P. B. Mussel-Inspired Surface Chemistry for Multifunctional Coatings. *Science* **2007**, *318*, 426−430.
(37) Lee, H.; Rho, J.; Messersmith, P. B. Facile Conjugation of Biomolecules onto Surfaces via Mussel Adhesive Protein Inspired Coatings. *Adv. Mater.* **2009**, *21*, 431−434.
(38) Kumar, A.; Kumar, S.; Rhim, W.-K.; Kim, G.-H.; Nam, J.-M. Oxidative Nanopeeling Chemistry-Based Synthesis and Photodynamic and Photothermal Therapeutic Applications of Plasmonic Core-Petal Nanostructures. *J. Am. Chem. Soc.* **2014**, *136*, 16317−16325.
(39) Yang, S.; Zhang, F.; Liang, Q.; Wang, Z. A Three-Dimensional Graphene-Based Ratiometric Signal Amplification Aptasensor for MUC1 Detection. *Biosens. Bioelectron.* **2018**, *120*, 85−92.
(40) Zhou, J.; Wang, P.; Wang, C.; Goh, Y. T.; Fang, Z.; Messersmith, P. B.; Duan, H. Versatile Core-Shell Nanoparticle@ Metal-Organic Framework Nanohybrids: Exploiting Mussel-Inspired Polydopamine for Tailored Structural Integration. *ACS Nano* **2015**, *9*, 6951−6960.
(41) Wu, H.; Chua, Y. S.; Krungleviciute, V.; Tyagi, M.; Chen, P.; Yildirim, T.; Zhou, W. Unusual and Highly Tunable Missing-Linker Defects in Zirconium Metal-Organic Framework UiO-66 and Their Important Effects on Gas Adsorption. *J. Am. Chem. Soc.* **2013**, *135*, 10525−10532.
(42) Tsuruoka, T.; Furukawa, S.; Takashima, Y.; Yoshida, K.; Isoda, S.; Kitagawa, S. Nanoporous Nanorods Fabricated by Coordination Modulation and Oriented Attachment Growth. *Angew. Chem., Int. Ed.* **2009**, *48*, 4739−4743.
(43) Bloch, E. D.; Britt, D.; Lee, C.; Doonan, C. J.; Uribe-Romo, F. J.; Furukawa, H.; Long, J. R.; Yaghi, O. M. Metal Insertion in a Microporous Metal-Organic Framework Lined with 2,2′-Bipyridine. *J. Am. Chem. Soc.* **2010**, *132*, 14382−14384.
(44) Li, C.-H.; Chao, W.; Christoph, K.; Jing, Z.; Li, J.; Yang, S.; Peng, Z.; Yi, C.; Franziska, L.; Christian, L.; Xiao, Y.; Zhe, B. A Highly Stretchable Autonomous Self-Healing Elastomer. *Nat. Chem.* **2016**, *8*, 618−624.
(45) Wu, L.; Qu, X. Cancer Biomarker Detection: Recent Achievements and Challenges. *Chem. Soc. Rev.* **2015**, *44*, 2963−2997.
(46) Tan, K.; Nijem, N.; Canepa, P.; Gong, Q.; Li, J.; Thonhauser, T.; Chabal, Y. J. Stability and Hydrolyzation of Metal Organic Frameworks with Paddle-Wheel SBUs upon Hydration. *Chem. Mater.* **2012**, *24*, 3153−3167.
(47) Cheng, Z.; Liao, J.; He, B.; Zhang, F.; Zhang, F.; Huang, X.; Zhou, L. One-Step Fabrication of Graphene Oxide Enhanced Magnetic Composite Gel for Highly Efficient Dye Adsorption and Catalysis. *ACS Sustainable Chem. Eng.* **2015**, *3*, 1677−1685.
(48) Kim, H.; Lee, D.; Kim, J.; Kim, T.-i.; Kim, W. J. Photothermally Triggered Cytosolic Drug Delivery via Endosome Disruption Using a Functionalized Reduced Graphene Oxide. *ACS Nano* **2013**, *7*, 6735−6746.
(49) Liang, R.; Jing, F.; Shen, L.; Qin, N.; Wu, L. MIL-53(Fe) as a Highly Efficient Bifunctional Photocatalyst for the Simultaneous Reduction Of Cr(VI) and Oxidation of Dyes. *J. Hazard. Mater.* **2015**, *287*, 364−372.
(50) Tam, S. K.; Dusseault, J.; Polizu, S.; Ménard, M.; Hallé, J.-P.; Yahia, L. H. Physicochemical Model of Alginate-Poly-L-Lysine Microcapsules Defined at the Micrometric/Nanometric Scale Using ATR-FTIR, XPS, and Tof-SIMS. *Biomaterials* **2005**, *26*, 6950−6961.
(51) Das, S. K.; Bhunia, M. K.; Motin Seikh, M.; Dutta, S.; Bhaumik, A. Highly Porous Co(II)-Salicylate Metal-Organic Framework: Synthesis, Characterization and Magnetic Properties. *Dalton Trans.* **2011**, *40*, 2932−2939.
(52) Chandra, V.; Park, J.; Chun, Y.; Lee, J. W.; Hwang, I.-C.; Kim, K. S. Water-Dispersible Magnetite-Reduced Graphene Oxide Composites for Arsenic Removal. *ACS Nano* **2010**, *4*, 3979−3986.
(53) Ryu, J.; Ku, S. H.; Lee, H.; Park, C. B. Mussel-Inspired Polydopamine Coating as a Universal Route to Hydroxyapatite Crystallization. *Adv. Funct. Mater.* **2010**, *20*, 2132−2139.
(54) Fei, B.; Qian, B.; Yang, Z.; Wang, R.; Liu, W. C.; Mak, C. L.; Xin, J. H. Coating Carbon Nanotubes by Spontaneous Oxidative Polymerization of Dopamine. *Carbon* **2008**, *46*, 1795−1797.
(55) Qi, P.; Zhang, D.; Wan, Y. Morphology-Tunable Polydopamine Nanoparticles and Their Application in Fe^{3+} Detection. *Talanta* **2017**, *170*, 173−179.
(56) Sun, D. T.; Gasilova, N.; Yang, S.; Oveisi, E.; Queen, W. L. Rapid, Selective Extraction of Trace Amounts of Gold from Complex Water Mixtures with a Metal-Organic Framework (MOF)/Polymer Composite. *J. Am. Chem. Soc.* **2018**, *140*, 16697−16703.
(57) Liang, R.; Shen, L.; Jing, F.; Qin, N.; Wu, L. Preparation of MIL-53(Fe)-Reduced Graphene Oxide Nanocomposites by a Simple Self-Assembly Strategy for Increasing Interfacial Contact: Efficient Visible-Light Photocatalysts. *ACS Appl. Mater. Interfaces* **2015**, *7*, 9507−9515.
(58) Wang, Y.-R.; Hu, P.; Liang, Q.-L.; Luo, G.-A.; Wang, Y.-M. Application of Carbon Nanotube Modified Electrode in Bioelectroanalysis. *Chin. J. Anal. Chem.* **2008**, *36*, 1011−1016.
(59) Kavosi, B.; Salimi, A.; Hallaj, R.; Moradi, F. Ultrasensitive Electrochemical Immunosensor for PSA Biomarker Detection in Prostate Cancer Cells Using Gold Nanoparticles/PAMAM Den-

https://dx.doi.org/10.1021/acsami.9b19161
ACS Appl. Mater. Interfaces 2020, 12, 5500−5510

drimer Loaded with Enzyme Linked Aptamer as Integrated Triple Signal Amplification Strategy. *Biosens. Bioelectron.* **2015**, *74*, 915−923.
(60) Chen, Y.; Wang, A.-J.; Yuan, P.-X.; Luo, X.; Xue, Y.; Feng, J.-J. Three Dimensional Sea-Urchin-Like Pdaucu Nanocrystals/Ferrocene-Grafted-Polylysine as an Efficient Probe to Amplify the Electrochemical Signals for Ultrasensitive Immunoassay of Carcinoembryonic Antigen. *Biosens. Bioelectron.* **2019**, *132*, 294−301.
(61) Liu, J.; Wang, J.; Wang, T.; Li, D.; Xi, F.; Wang, J.; Wang, E. Three-Dimensional Electrochemical Immunosensor for Sensitive Detection of Carcinoembryonic Antigen Based on Monolithic and Macroporous Graphene Foam. *Biosens. Bioelectron.* **2015**, *65*, 281−286.
(62) Gao, Z.; Li, Y.; Zhang, X.; Feng, J.; Kong, L.; Wang, P.; Chen, Z.; Dong, Y.; Wei, Q. Ultrasensitive Electrochemical Immunosensor for Quantitative Detection of Hbeag Using Au@Pd/Mos_2@Mwcnts Nanocomposite as Enzyme-Mimetic Labels. *Biosens. Bioelectron.* **2018**, *102*, 189−195.
(63) Chen, J. R.; Jiao, X. X.; Luo, H. Q.; Li, N. B. Probe-Label-Free Electrochemical Aptasensor Based on Methylene Blue-Anchored Graphene Oxide Amplification. *J. Mater. Chem. B* **2013**, *1*, 861−864.
(64) Wang, Q.-L.; Cui, H.-F.; Song, X.; Fan, S.-F.; Chen, L.-L.; Li, M.-M.; Li, Z.-Y. A Label-Free and Lectin-Based Sandwich Aptasensor for Detection of Carcinoembryonic Antigen. *Sens. Actuators, B* **2018**, *260*, 48−54.
(65) Zhou, J.; Du, L.; Zou, L.; Zou, Y.; Hu, N.; Wang, P. An Ultrasensitive Electrochemical Immunosensor for Carcinoembryonic Antigen Detection Based on Staphylococcal Protein A-Au Nanoparticle Modified Gold Electrode. *Sens. Actuators, B* **2014**, *197*, 220−227.
(66) Guo, A.; Wu, D.; Ma, H.; Zhang, Y.; Li, H.; Du, B.; Wei, Q. An Ultrasensitive Enzyme-Free Electrochemical Immunosensor for CA125 Using Au@Pd Core-Shell Nanoparticles as Labels and Platforms for Signal Amplification. *J. Mater. Chem. B* **2013**, *1*, 4052−4058.
(67) Huang, J.-Y.; Zhao, L.; Lei, W.; Wen, W.; Wang, Y.-J.; Bao, T.; Xiong, H.-Y.; Zhang, X.-H.; Wang, S.-F. A High-Sensitivity Electrochemical Aptasensor of Carcinoembryonic Antigen Based on Graphene Quantum Dots-Ionic Liquid-Nafion Nanomatrix and Dnazyme-Assisted Signal Amplification Strategy. *Biosens. Bioelectron.* **2018**, *99*, 28−33.

https://dx.doi.org/10.1021/acsami.9b19161
ACS Appl. Mater. Interfaces 2020, 12, 5500−5510